mater.scichina.com link.springer.com

Sci China Mater 2026, 69(1): 374–383
https://doi.org/10.1007/s40843-025-3715-5

Molecularly engineered porphyrin photosensitizers featuring multi-anchoring and alkoxy modifications for robust photocatalytic hydrogen production

Yudong Wen[1,2], Cheuk-Lam Ho[1,2*] and Yan Yi Kwok[1,2]

ABSTRACT **In this work, we introduce a new generation of porphyrin-based photosensitizers (PSs), PoTA1–PoTA3, each strategically engineered with dual anchoring groups—4-ethynylbenzoic acid, 3-ethynylbenzoic acid, or 5-ethynylthiophene-2-carboxylic acid—at the *meso*-position of the porphyrin macrocycle, and further functionalized with long-chain alkyloxy substituents. This dual-modification strategy not only suppresses undesirable charge recombination but also reduces aggregation on TiO_2 surfaces. Notably, PoTA3, featuring the 5-ethynylthiophene-2-carboxylic acid moiety, exhibits a dramatically redshifted and broadened absorption profile, enabling superior solar spectrum utilization. Under blue light irradiation, the PoTA3-based system achieves a remarkable apparent quantum yield (AQY) of 8.3%, an initial hydrogen evolution rate of 485 mmol g^{-1} h^{-1}, and an exceptional turnover number (TON) of 27,858 in aqueous media—substantially outperforming both PoTA1 and PoTA2. More notably, both PoTA1 and PoTA3 exhibit remarkable performance under white light irradiation (AQY% = 5.5% and 6.8%, respectively), significantly outperforming the benchmark YD2-*o*-C8 (AQY% = 4.07%) under identical operating conditions. The synergistic effect of enhanced light harvesting, minimized aggregation, and optimized HOMO and LUMO electron density distributions in PoTA1 and PoTA3 translates to both high efficiency and robust operational stability. These findings create a flexible molecular engineering platform for the next generation of solar-to-hydrogen conversion systems. Our approach opens the door to designing better photosensitizers, which could lead to major improvements in producing hydrogen from water using sunlight.**

Keywords: hydrogen, photocatalysis, photosensitizers, porphyrins

INTRODUCTION

To meet the surging demand for energy and resources needed for social and technological advancements, environmental concerns – such as global warming triggered by the emission of greenhouse gases from burning fossil fuels – and the restricted availability of fossil fuels, have brought sustainable, renewable, and clean energy with notably high efficiency into the forefront of chemistry research in recent years [1,2]. Hydrogen emerges as a clean energy source with diverse applications, ranging from automotive power and heating to fuel cells and beyond, providing a reduced environmental impact as its combustion produces only water [3]. Furthermore, the use of hydrogen as an alternative fuel embodies a longstanding approach to worldwide carbon dioxide emission reduction [4,5]. However, the current practical source of hydrogen production is reforming fossil fuels, which is a finite energy source on Earth and causes environmental problems by releasing carbon dioxide during its combustion [6]. Indeed, hydrogen can be produced catalytically from water through a solar-driven photocatalytic process [7–10]. This process, while conceptually straightforward, requires efficient and affordable photocatalysts to attain practical viability. Noble metal-free molecular photocatalysts are attracting increasing attention in recent years, owing to their potential advantages in regard to abundant material availability, low toxicity, and tunable molecular structure [11–14]. Among these, porphyrins, as tetrapyrrolic compounds closely resembling chlorophyll utilized in plant photosynthesis, serve as an ideal model for gathering solar energy in photocatalytic hydrogen evolution (PHE) systems. This is due to their analogous function in the natural process of photosynthesis and their photostable [15]. The conjugated π-electron system of porphyrins allows for the efficient absorption of visible-spectrum solar radiation [7,15–18]. Crucially, porphyrins facilitate both electron transfer and energy conversion during photosynthesis. Therefore, porphyrin-based photocatalysts have emerged as a focal point of research within PHE systems.

Porphyrins possess a rigid, planar macrocyclic structure, which, while advantageous for π-conjugation, renders them susceptible to π–π stacking aggregation. This aggregation can significantly impede electron injection efficiency into semiconductor materials such as TiO_2 [19]. Strategic modification of substituents at the *meso*- or *β*-positions of the porphyrin ring offers a versatile approach to tuning their physicochemical properties, including solubility, stability, and optical characteristics. Notably, the introduction of long alkyloxy chain ortho-substituted aryl groups at the *meso* positions has proven effective in disrupting π–π stacking, thereby mitigating aggregation. This structural modification not only preserves the integrity of the porphyrin framework but also provides a shielding effect that suppresses undesirable electron back-transfer from the TiO_2 conduction band to the electrolyte [20,21]. Further enhancement

[1] Department of Applied Biology and Chemical Technology, The Hong Kong Polytechnic University, Hong Kong 999077, China
[2] PolyU Shenzhen Research Institute, Shenzhen 518057, China
[*] Corresponding author (email: cheuk-lam.ho@polyu.edu.hk)

of charge separation can be achieved by judiciously engineering electron-donating and electron-accepting substituents on the porphyrin core, thereby intensifying light-harvesting capabilities and promoting efficient charge transfer [22]. Anchoring groups are equally essential, as they facilitate robust grafting of porphyrin photosensitizers onto TiO_2 surfaces, which is critical for rapid electron injection during PHE from water [23]. The incorporation of carboxylic acid groups at the *β*- and *meso*-positions has been extensively explored [24,25], with *meso*-substituted benzoic acid or alkynylbenzoic acid (serving as π-linkers) being particularly prevalent. The positional isomerism of the carboxyl group (*meta* versus *para*) on these phenyl rings can markedly influence photocatalytic performance by modulating electronic communication between the porphyrin and the semiconductor, thereby facilitating more efficient electron injection across the PS–TiO_2 interface [26,27]. Additionally, the electronic nature of the π-linker itself plays a pivotal role in mediating charge transfer between the photosensitizer core and TiO_2, further impacting overall photocatalytic efficiency [28–30].

In 2018, our group reported that the Zn(II) porphyrin-based PSs **YD2-*o*-C8** and **ZnP-dyad** achieved outstanding PHE performances from water: initial turnover frequency (TOF_i) > 300 h^{-1} under white light irradiation and initial apparent quantum yield percentage (AQY_i%) up to 4.07% (Fig. 1) [31]. To broaden our scope of investigation, a set of porphyrin-based PSs (**PoTA1**–**PoTA3**) has been synthesized for PHE from water. These photosensitizers are meticulously engineered with dual anchoring motifs—either 4-ethynylbenzoic acid, 3-ethynylbenzoic acid, or 5-ethynylthiophene-2-carboxylic acid—strategically tethered at the *meso*-positions of the porphyrin macrocycle. To further optimize their performance, each PS is deliberately endowed with long-chain alkyloxy substituents, effectively suppressing unwanted charge recombination and mitigating aggregation on TiO_2 surfaces. In a smart design, pyridyl groups are also incorporated into the porphyrin scaffold, introducing additional anchoring sites and expanding the interfacial versatility of these advanced PSs. The photophysical, electrochemical, and photocatalytic characteristics of these PSs are comprehensively explored to elucidate their structure–function relationships. Recognizing the broad spectral range of solar irradiation, we strategically employ white LED illumination as one of the representative light sources, enabling a more realistic assessment of the PSs' performance under conditions that closely mimic natural sunlight. Notably, **PoTA1** and **PoTA3** attained an active and robust H_2 generation system over 150 h for blue, green, and white irradiation, with the TON of up to 17780 and 24200 in 168 and 173 h with 26.8 and 36.6 mL hydrogen produced under white light irradiation. Their initial turnover frequency (TOF_i) was 518 and 640 h^{-1}, the initial activity ($activity_i$) was 324 and 400 mmol g^{-1} h^{-1}, and the initial apparent quantum yield (AQY_i) was 5.5 and 6.8%, under visible light irradiation from water. The results reveal that introducing an alkoxyl chain onto the pyridine moiety at the *meso*-position of the porphyrin markedly amplifies PHE efficiency in aqueous systems, with the positional variation of the carboxylic acid on the ethynyl benzoic acid further modulating this effect. The incorporation of extended alkoxy chains is particularly impactful, as it promotes intramolecular charge transfer, effectively suppresses dye aggregation, and enhances the structural stability of the porphyrin framework. Moreover, electrochemical impedance spectroscopy (EIS) confirms that these modifications significantly retard charge recombination dynamics during PHE, collectively contributing to superior photocatalytic performance [21,32–35]. Thus, by synergistically integrating extended alkoxyl

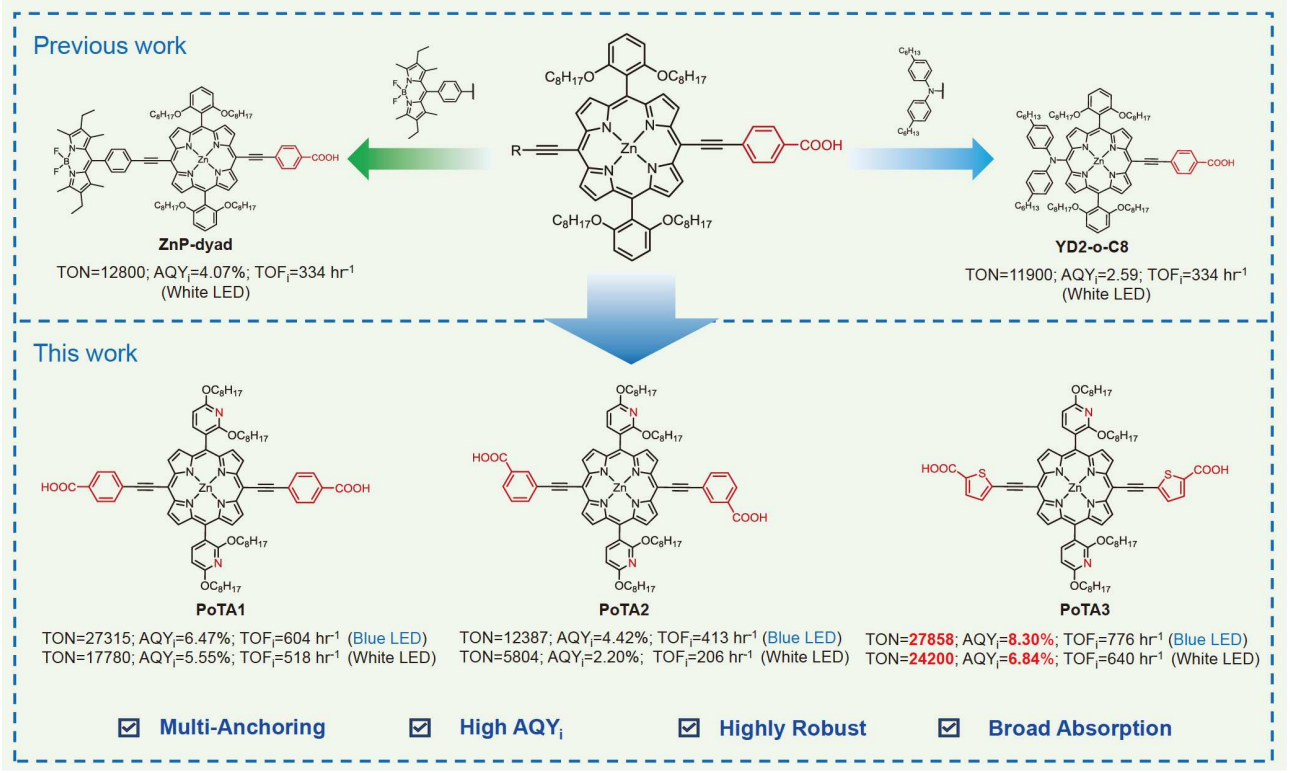

Figure 1 The molecular structures design strategy of **PoTA1**, **PoTA2**, and **PoTA3**.

chains with multiple anchoring groups on the porphyrin framework, a platform that simultaneously maximizes light-harvesting capabilities and elevates the photocatalytic efficiency of PSs can be established, setting a new paradigm for advanced solar-driven hydrogen production systems.

RESULTS AND DISCUSSION

Synthesis and structural characterization

The structures of the new porphyrin-based PSs are displayed in Fig. 1, while their synthetic routes are illustrated in Scheme 1. 2,6-Dichloropyridine first underwent functionalization with octanol to produce 2,6-bis(octyloxy)pyridine **1**, subsequently leading to aldehyde formation, resulting in 2,6-bis(octyloxy) nicotinaldehyde **2**. The key intermediate **4** was then prepared by the cyclization of porphyrin, using dipyrrolemethane **3** to react with **2** in dry CH_2Cl_2 under a nitrogen atmosphere. Trifluoroacetic acid (TFA) was used as the acid for initiating the condensation, while 2,3-dichloro-5,6-dicyano-1,4-benzoquinone (DDQ) was added to oxidize the ring after the cyclization. This two-step synthesis could prevent side reactions during the porphyrin formation. Bromination of **4** by using *N*-bromosuccinimide gave **5**. The brominated porphyrin was metalated using zinc acetate in refluxing dichloromethane/methanol solution to give **6**. Sonogashira cross-coupling reaction was performed by employing palladium catalyst and copper catalyst to form a carbon-carbon triple bond between the terminal alkyne and the aryl halide, under basic conditions mediated by triethylamine to give targeted **PoTA1**–**PoTA3**.

The target porphyrin-based PSs and their precursors are soluble in common solvents, like dichloromethane, dimethyl sulfoxide, tetrahydrofuran, etc., and were characterized by ^{1}H NMR spectroscopy and Electrospray Ionization Quadrupole-Time-of-Flight Mass Spectrometer (ESI-TOF-MS). However, the acquisition of good-quality ^{13}C NMR spectra of porphyrin-based PSs was difficult due to their partial solubility in common organic solvents.

In these porphyrin-based PSs, their molecular structures comprise two 4-ethynylbenzoic acid, 3-ethynylbenzoic acid, or 5-ethynylthiophene-2-carboxylic acid tethered at the 10,20-*meso*-positions of the porphyrin core, along with 2,6-dioctylpyridine at the 5,15-*meso*-position. This combination could potentially tetrachelate since both pyridine and carboxylic acid could bind to the Brønsted and Lewis acid sites of TiO_2,

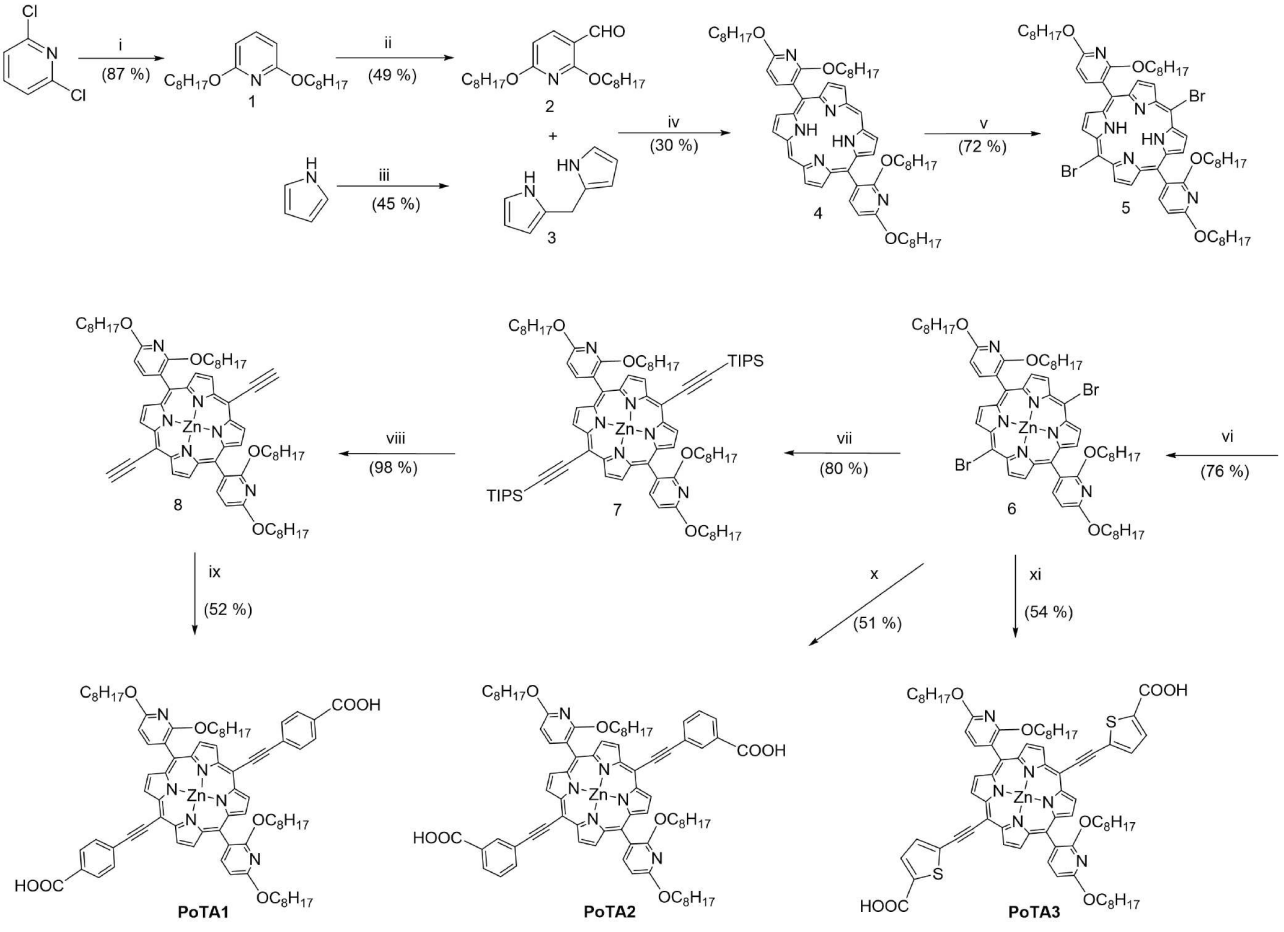

Scheme 1 Synthesis of **PoTA1**–**PoTA3**: i) Sodium hydride, octanol, 2,6-dichloropyridine; ii) *n*-butyl lithium, dry tetrahydrofuran (THF), dry Dimethylformamide (DMF); iii) Paraformaldehyde, pyrrole, indium chloride, NaOH solution; iv) Trifluoroacetic acid (TFA), 2,3-dichloro-5,6-dicyano-1,4-benzoquinone (DDQ), anhydrous dichloromethane; v) *N*-Bromosuccinimide (NBS), anhydrous CH_2Cl_2; vi) zinc acetate, CH_2Cl_2:methanol 2:1; vii) (Triisopropylsilyl)acetylene, copper(I) iodide, $Pd(PPh_3)_2Cl_2$, NEt_3, anhydrous THF; viii) Tetrabutylammonium fluoride (TBAF), anhydrous THF; ix) 4-Iodobenzoic acid, $Pd_2(dba)_3$, $AsPh_3$, NEt_3, anhydrous THF; x) 3-Ethynyl benzoic acid, $Pd(PPh_3)_2Cl_2$, CuI, NEt_3, anhydrous THF; xi) 5-Ethynylthiophene-2-carboxylic acid, $Pd(PPh_3)_4$, CuI, NEt_3, anhydrous THF.

respectively [36]. To investigate the binding modes of these porphyrins on the TiO_2 surface, Fourier-transform infrared (FTIR) spectroscopic data were obtained for the pure solid of the selected PS, **PoTA3**, and for the PS adsorbed on TiO_2. Their FTIR spectra are compared in Fig. S30. The FTIR spectrum of **PoTA3** displayed the stretching vibration bands of the C=O stretching band of the carboxyl group, C=C, and C–N at 1671, 1596, and 1456 cm^{-1}. After the dye-loading onto TiO_2, the spectrum illustrated the absence of the C=O stretching band at 1671 cm^{-1}. This observation suggests that this type of PSs can be effectively anchored onto the surface of TiO_2 nanoparticles covalently through an ester linkage at the Brønsted acid sites (surface-bound hydroxyl groups) [37]. Another new peak appeared at approximately 1636 cm^{-1}, which corresponds to the coordination of the pyridine ring with the Lewis acid sites on the TiO_2 surface (the exposed Ti^{n+} cations) [38,39]. This data suggests that both carboxylic acid and pyridyl groups are attached to the TiO_2 surface [40–42].

Photophysical properties

The ultraviolet-visible (UV-vis) absorption and photoluminescence (PL) spectra of all porphyrin-based PSs were measured in dichloromethane and presented in Fig. 2, with the corresponding data tabulated in Table 1. All the UV-visible spectra of our PSs in solution exhibit the characteristic peak of porphyrin compounds: a prominent absorption peak within the 400–500 nm range, known as the Soret band absorption. Additionally, we observe several absorption peaks of moderate intensity between 525 and 700 nm, corresponding to the Q band absorption [43]. The appearance of the former absorption band is ascribed to the π-π* electronic transition within the porphyrin molecule, while the emergence of the latter absorption band is due to intramolecular charge transfer (ICT) within the porphyrin structure [44,45]. There was a bathochromic shift of **PoTA3** (λ_{max} = 459 nm) >**PoTA1** (λ_{max} = 453 nm) > **PoTA2** (λ_{max} = 448 nm) in the Soret band, while their ε was in the trend of **PoTA3** (204519 M^{-1} cm^{-1}) > **PoTA2** (157474 M^{-1} cm^{-1}) > **PoTA1** (146227 M^{-1} cm^{-1}). This Zn-porphyrin series has been able to effectively shift the main peak in the Q-band to a wavelength of λ_{max} = 651–668 nm, achieving ε up to 42300 M^{-1} cm^{-1}. Hence, substituting ethynyl benzoic acid with 5-ethynylthiophene-2-carboxylic acid could effectively red-shift both the Soret and Q-bands while also boosting the ε. This change suggests that the excited state becomes more polar than the ground state by incorporating the thiophene unit as a π-spacer [46,47]. This outcome illustrates that the heteroaromatic unit (specifically thiophene serving as the π-spacer) exerts a notable influence on the absorption spectra of porphyrin PSs. Furthermore, shifting the COOH group from the *para*- to the *meta*-position on the phenyl linker results in a blue shift observed in the absorption wavelengths of both the Soret and Q-bands. Such a phenomenon is due to the inductive effect. The carboxyl group at the *para*-position of phenyl contributes more π-electrons in conjugation, leading to the bathochromic shift of both bands in **PoTA1**. These findings suggest that the positioning of the COOH moiety on the phenyl linker connected to the porphyrin ring significantly influences the absorption properties of isomeric porphyrins.

All the porphyrins demonstrated photoluminescence in dichloromethane at room temperature. Each of them displays two emission peaks: a strong peak at approximately 660–678 nm and a shoulder peak at around 717–742 nm when excited at 450 nm (Fig. 2b). The trend in emission redshift mirrors the trend observed in their Q-band absorption spectra. The emission spectrum of **PoTA3** exhibits a further red-shifted feature, pointing towards a more effective electronic coupling between 5-ethynylthiophene-2-carboxylic acid and the porphyrin ring.

Ultraviolet-visible diffuse reflectance spectroscopy (UV-Vis DRS) was also conducted on the three solid powder samples of PSs (Fig. 2c). All samples demonstrated analogous light

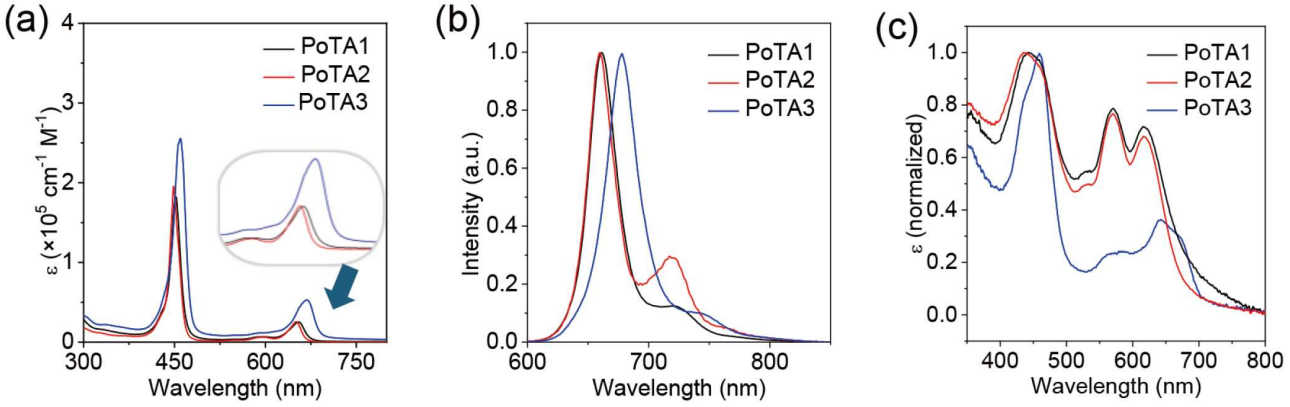

Figure 2 (a) UV/Vis absorption spectra in CH_2Cl_2 at 293 K; (b) Normalized photoluminescence spectra in CH_2Cl_2 at 293 K; (c) Normalized UV-Vis diffuse reflectance spectra of **PoTA1**–**PoTA3**.

Table 1 UV/Vis absorption data and emission data of **PoTA1**–**PoTA3** in CH_2Cl_2

PS	λ_{max}/nm (ε/M^{-1} cm^{-1})		λ_{em}/nm
	Soret band	Q-band	
PoTA1	453 (146227)	551 (2887), 596 (5386), 655 (20238)	661, 720
PoTA2	448 (157474)	548 (2021), 596 (5093), 651 (20368)	660, 717
PoTA3	459 (204519)	552 (6930), 593 (9284), 668 (42385)	678, 742

absorption characteristics in the solid state, mirroring those observed in dichloromethane solution, with consistent absorption features within the 400–500 nm range. Intriguingly, a novel absorption peak emerged around 600 nm in the solid-state spectra, entirely absent in the solution phase. This phenomenon is attributable to robust electronic coupling between molecules and the formation of orderly stacked structures in the aggregated state, giving rise to distinctive electronic transition behavior unique to the solid state.

Electrochemical properties

Optimizing the energy gap between the TiO_2 semiconductor, SED, and zinc(II) porphyrins is essential for achieving efficient PHE [48]. The effectiveness of electron transfer and charge separation in these complexes relies on the LUMO energy level being above the semiconductor's conduction band, while the HOMO level must be below that of the SED. To map out the energy profiles of the porphyrins, cyclic voltammetry was performed using a standard three-electrode system. The specific parameters obtained from these experiments are summarized in Table 2.

The E_{HOMO} of these PSs (ranging from −5.299 to −5.219 eV) were all more negative than the redox potential energy level (−4.65 eV, pH ≈ 4) of ascorbic acid [49] (AA; acting as the sacrificial electron donor in the H_2 production experiment) and their corresponding E_{LUMO} (ranging from −3.238 to −3.338 eV) were all higher than the conduction band energy level (about −4.26 eV) of TiO_2 nanoparticles [50]. Consequently, effective dye regeneration [51] and electron injection [52] were both anticipated to occur in the photocatalytic H_2 generation cycle.

Theoretical calculation

Theoretical simulations were conducted using density functional theory (DFT) at the B3LYP/6-31g(d)/LANL2DZ level. The optimized geometries, energy levels, and electron density distributions are shown in Fig. 3. The three porphyrin complexes exhibit slight variances in the energy levels of the highest occupied molecular orbital (HOMO), ranging from −5.13 to −5.02 eV. The electron cloud of the HOMO is delocalized over the porphyrin ring and the conjugated aromatic π-linkers. For the lowest unoccupied molecular orbital (LUMO), the energy levels range from −2.92 to −2.68 eV, with electron cloud distribution similar to that of the HOMO. To gain deeper insight into the nature of the excited states, natural transition orbital (NTO) analysis was performed to explore the characteristics of the excited states in the three porphyrin complexes (Fig. 4). Both the singlet and triplet excited states of the three porphyrin complexes exhibit LE characteristics. As shown in Fig. 5, the

Table 2 Electrochemical data and energy levels for **PoTA1**–**PoTA3**

PS	E_{ox}/V[a]	E_{HOMO}/eV[b]	$E_{0\text{-}0}$/eV[c]	E_{LUMO}/eV[d]
PoTA1	0.589	−5.299	1.981	−3.318
PoTA2	0.509	−5.219	1.981	−3.238
PoTA3	0.581	−5.291	1.953	−3.338

a) Onset of first oxidation potentials were measured by cyclic voltammetry in dichloromethane (CH_2Cl_2) solution containing 0.1 M of NBu_4PF_6 against Ag/Ag^+ reference electrode, with glassy carbon working electrode and platinum wire auxiliary electrodes.
b) Calculated from $-(E_{ox} + 4.71)$, as reversible oxidation of ferrocene was $E_{1/2}$ = 0.09 V and the E_{HOMO} of ferrocene is equal to −4.80 eV vs. to vacuum level.
c) $E_{0\text{-}0}$ was determined from the intersection of absorption and emission spectra.
d) $E_{LUMO} = E_{HOMO} + E_{0\text{-}0}$.

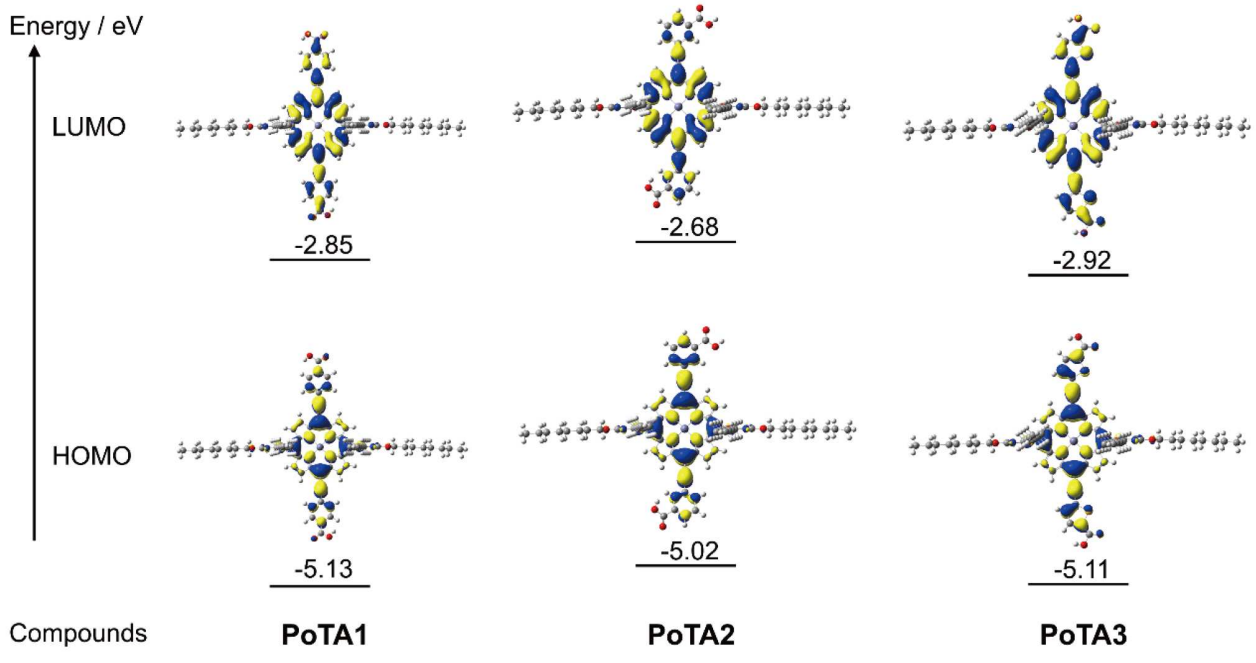

Figure 3 Calculated energy-level diagram and contour plots of the HOMO and LUMO for **PoTA1**, **PoTA2**, and **PoTA3**.

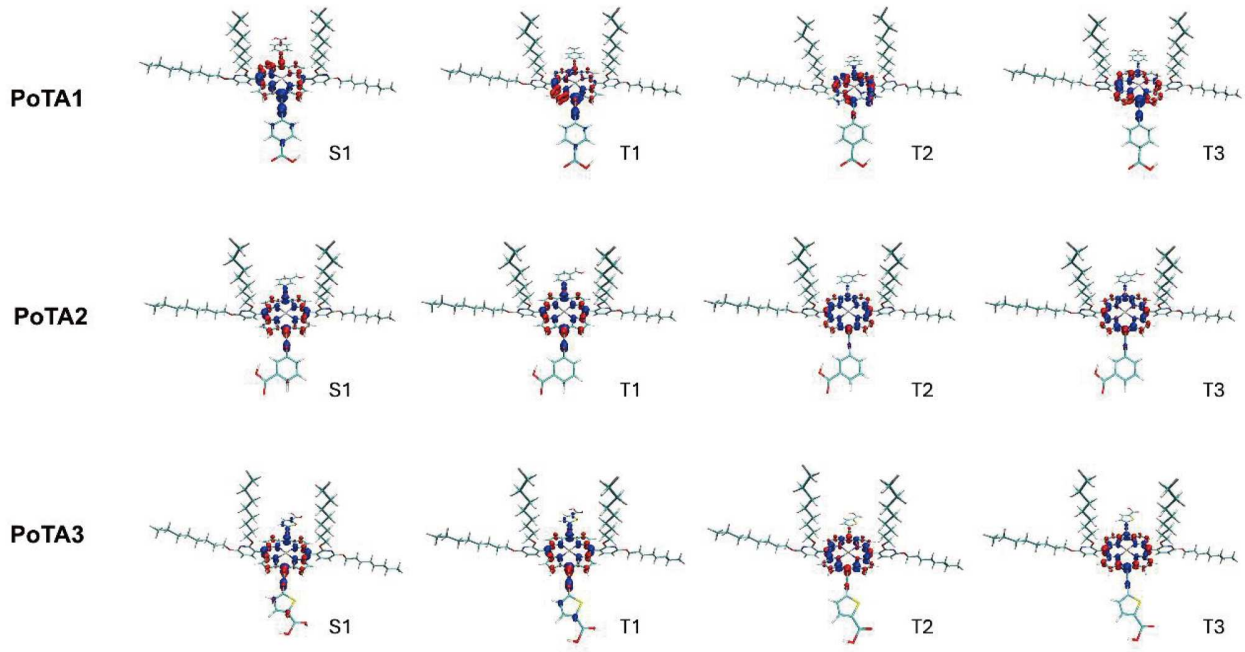

Figure 4 NTOs describing the characters of excited singlet (S_1) and triplet (T_m) states (hole: blue color; particle: red color).

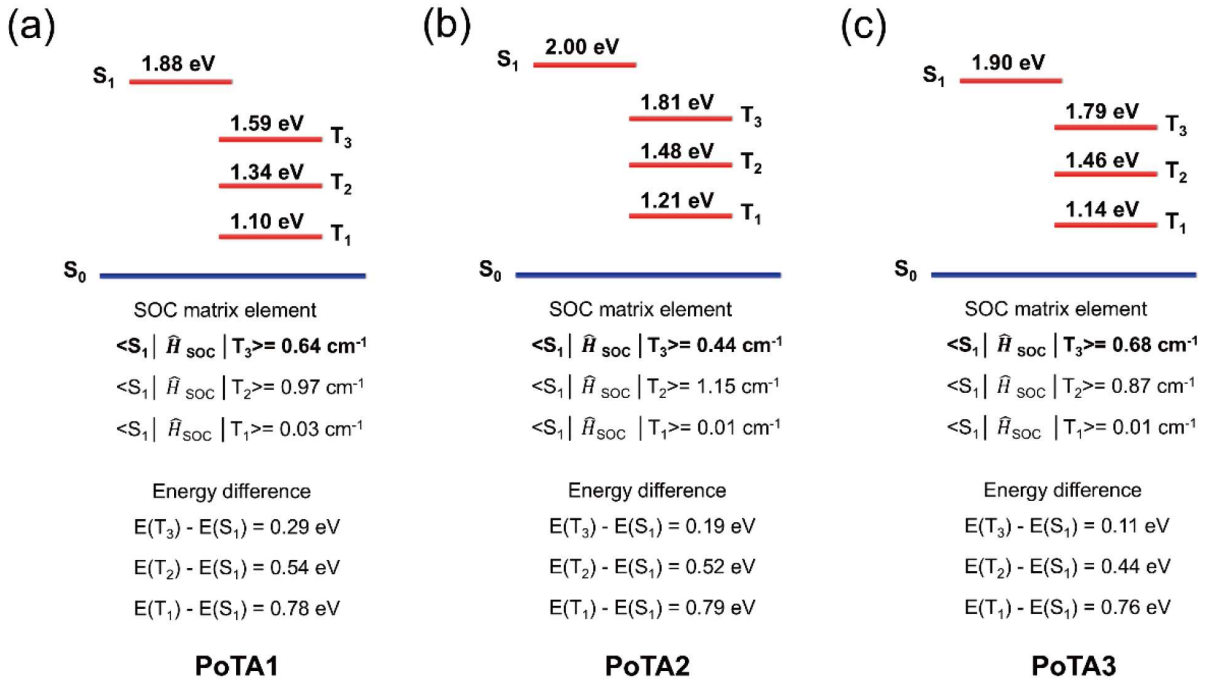

Figure 5 Energy-level diagram for the excited singlet (S_1) and triplet (T_m) states. SOC matrix elements and energy difference between the T_m and S_1 states of (a) **PoTA1**, (b) **PoTA2**, and (c) **PoTA3**.

singlet-triplet energy gap (ΔE_{ST}) ranges from 0.76 to 0.79 eV. Notably, the S_1 state of the **PoTA3** molecule shows the smallest energy difference with the T_3 state compared to **PoTA1** and **PoTA2**, with a spin-orbit coupling (SOC) value reaching 0.68 cm^{-1}. This significantly enhanced SOC effect is attributed to the heavy atom effect of the sulfur atom in the thiophene linkers, where the larger atomic radius effectively promotes the inter-system crossing (ISC) process by enhancing spin-orbit interaction.

In the study of interfacial binding characteristics, the interaction capability between the PSs and TiO_2 was assessed by calculating the binding energy at a single anchoring point. The results indicate that the pyridine groups of the three PSs bind more effectively to TiO_2 compared to the carboxylic acid

anchoring groups, with TiO_2-pyridine binding energies ranging from −239.59 to −297.51 kJ mol^{-1} (as shown in Fig. S31 and Table S1). Notably, **PoTA3** exhibits the most prominent interfacial binding characteristics, with its pyridine-TiO_2 binding energy reaching the highest value in the system at −297.51 kJ mol^{-1}, while the carboxylic acid group binding energy is the lowest among the three. This significant reverse trend suggests that **PoTA3** has a specific binding tendency on the TiO_2 surface, preferring stable anchoring through the pyridine group. The results align with the FTIR results for **PoTA3** (Fig. S30), providing a clue that the pyridine coordination to the Lewis acid site of TiO_2 exists, despite the potential steric hindrance from the adjacent long alkoxy chains near the N of pyridine.

Electrochemical impedance spectroscopy and photocurrent response measurements

To provide more evidence for the explanation of photocatalytic electron transfer, the photocurrent responses and electrochemical impedance spectroscopy (EIS) of the porphyrins coated on fluorine-doped tin oxide (FTO) were performed. As shown in Fig. 6a, **PoTA3** exhibited a higher photocurrent than the other PSs, **PoTA1** and **PoTA2**, indicating more electrons generated and more efficient separation of photogenerated charge carriers in **PoTA3**. Also, the smaller transfer resistance of **PoTA3** (Fig. 6b) further supports its better charge transfer compared to other porphyrins.

Photocatalytic hydrogen production

Given the attractive light-harvesting capacity of the PSs within the 420–700 nm range, it is conceivable that these porphyrin-based PSs possess significant potential for efficient PHE from water. It has been previously reported in other works that dyads with platinum used as PSs could increase the efficiency and stability of generating hydrogen [53–55]. The procedures of platinizing TiO_2, PS-loading onto TiO_2, and measuring the volume of generated hydrogen are stated in the Experimental Section. The percentage of dye-loading on TiO_2 is measured by the change in absorbance of the PSs solution before and after the adsorption (Fig. S32) [56,57]. All the PSs achieved a high dye-loading percentage (>91%) with the potential to be in a tetra-chelated mode. The photocatalytic hydrogen generation system was executed in 5 mL 0.8 M aqueous ascorbic acid (pH 4.0), serving as the sacrificial electron donor (SED), under the irradiation of blue, green, or white LEDs. Upon comparing the reaction mixture before and after irradiation, the aqueous ascorbic acid solution transitioned from colorless to a deep yellow hue due to the formation of dehydroascorbic acid during the regeneration of the PSs in the photocatalytic process.

The hydrogen generation fitting curves for all synthesized porphyrin-based PSs are depicted in Fig. 7, along with the corresponding data (TON, TOF, TOF_i, $Activity_i$, and AQY_i%) in Table 3. All the PSs facilitated the photocatalytic hydrogen evolution, ranging from 18.7 to 42.2 mL, when compared to the control bare Pt-TiO_2 (4.9 mL) under blue light irradiation for over 189 h. There was a significant increase in hydrogen production for **PoTA1** and **PoTA3** within the initial 21 h across all three types of light. Their exceptional reactivity extended up to 50 and 100 h under blue and white LED lights, respectively.

The PHE system with **PoTA3** had the highest and most remarkable initial photocatalytic activity, with the initial apparent quantum yield % (AQY_i%) of 8.3% and the initial hydrogen production activity ($activity_i$) of 485 mmol g^{-1} h^{-1} under blue light irradiation, followed by **PoTA1** (AQY_i% = 6.5% and $activity_i$ = 378 mmol g^{-1} h^{-1}) and **PoTA2** (AQY_i% = 4.4% and $activity_i$ = 258 mmol g^{-1} h^{-1}). However, the later performance of **PoTA1** up to 189 h surpassed **PoTA3** (41.2 mL for **PoTA1** at 189 h and 42.026 mL for **PoTA3** at 194 h). Interestingly, **PoTA3** maintained higher activity after 189 h, evident from the steeper slope in Fig. 7a. On the contrary, the trend of prolonged performance between **PoTA1** and **PoTA3** was reversed under green light, with the order of AQY_i% being **PoTA3** (1.60%) > **PoTA1** (1.18%) > **PoTA2** (0.503%). However, **PoTA1** maintained higher activity under prolonged green light irradiation, displaying an increasing trend up to 360 h (Fig. 7b). The more reactive initial performances of **PoTA3** could be explained by its higher molar absorptivity throughout the visible light region than the other analogs, as well as the potentially smaller band gap of having 5-ethynylthiophene-2-carboxylic acid than 4-ethynyl benzoic acid [58], may facilitate more rapid electron injection from the PSs to the TiO_2. This factor notably assisted **PoTA3** in attaining a superior outcome under white light irradiation, showcasing its prowess as a PS with good panchromatic capability (Fig. 7c). Both the **PoTA1** and **PoTA3** had distinctive performances under white light irradiation, with the AQY_i% = 5.5% and 6.8%, respectively, and surpass that of

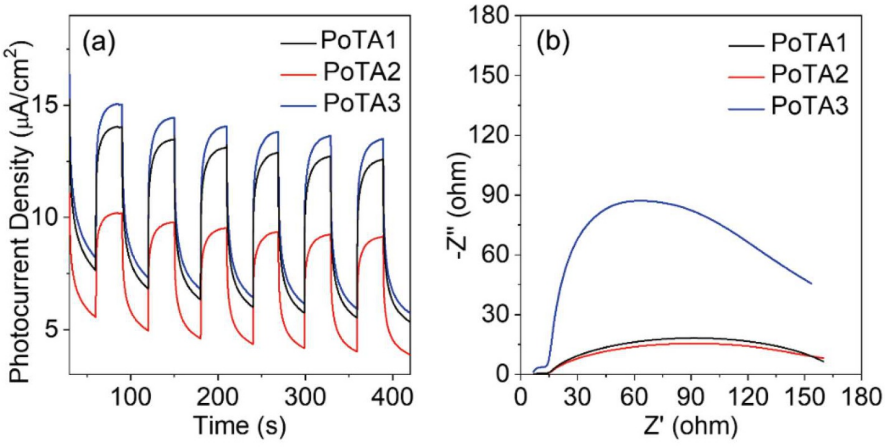

Figure 6 (a) Photocurrent responses and (b) EIS spectra of **PoTA1**–**PoTA3**.

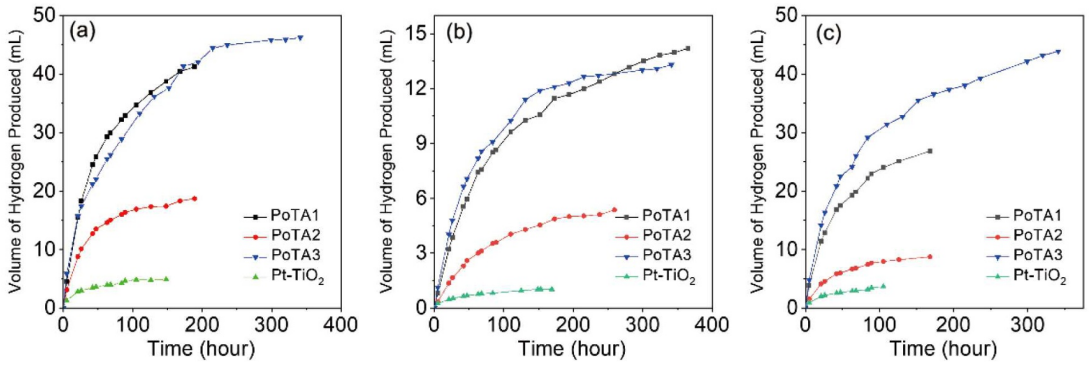

Figure 7 Kinetic traces of hydrogen generation by different photosensitizers (**PoTA1**–**PoTA3** and Pt-TiO_2) under the irradiation of (a) blue LED (472 nm); (b) green LED (520 nm) at 50 mW; (c) white LED (420–750 nm) at 80 mW. Each sample flask contained 0.8 M ascorbic acid (5 mL) in water (pH 4.0) and 20 mg PS-TiO_2-Pt sample.

Table 3 Light-Driven H_2 Generation Data with and without PSs **PoTA1**, **PoTA2**, and **PoTA3** on Pt-TiO_2

PS	DL%[a]	H_2/mL	TON[b]	TOF/(h^{-1})[c]	TOF_i/(h^{-1})[d]	$Activity_i$/(μmol g^{-1} h^{-1})[e]	AQY_i%[f]
Irradiation under blue LED (472 nm) for 189 h							
PoTA1	91	41.20	27315	144.521	604.328	377705	6.467
PoTA2	96	18.688	12387	65.5423	413.334	258334	4.423
PoTA3	97	42.026 (194 h)	27858 (194 h)	143.596 (194 h)	775.673	484796	8.301
Pt-TiO_2	-	4.8986	3247	19.2138	170.513	106571	1.825
Irradiation under green LED (520 nm) for 259 h							
PoTA1	91	14.201	9258	31.6607	110.679	69174	1.184
PoTA2	96	5.366	3387	13.0766	47.0091	29381	0.503
PoTA3	97	12.647 (215 h)	8384 (215 h)	38.9942 (215 h)	149.500	93468	1.600
Pt-TiO_2	-	1.030	683	4.04112	33.4168	20886	0.358
Irradiation under white LED (556 nm) for 168 h							
PoTA1	91	26.823	17780	105.208	518.303	323939	5.547
PoTA2	96	8.755	5804	34.3412	205.864	128665	2.203
PoTA3	97	36.508 (173 h)	24200 (173 h)	139.886 (173 h)	639.909	399943	6.848
Pt-TiO_2	-	3.6899	2446	15.6790	120.868	75543	1.293

a) Dye-loading percentage.
b) Turnover number of H_2 is calculated as 2 × number of moles of H_2 produced divided by the number of moles of PS attached to platinized TiO_2.
c) Turnover frequency is calculated per hour.
d) Initial turnover frequency in the first 5 h.
e) Initial photocatalytic activity of the system is defined as the number of micromoles of H_2 evolved per gram of platinum loaded per hour.
f) Initial apparent quantum yield percentage (AQY_i%) of the system.

YD2-*o*-C8 (AQY_i% = 4.07%) reported by our group [29]. The incorporation of long-chain alkoxy pyridyl groups into the porphyrin architecture dramatically suppresses aggregation on TiO_2 surfaces and substantially extends the operational stability of the PSs within photocatalytic systems. Collectively, these findings underscore the transformative potential of this molecular design, paving the way for next-generation PSs with enhanced panchromatic absorption and synergistic co-sensitization capabilities. This strategy holds considerable promise for driving further breakthroughs in PHE and solar energy conversion technologies.

Ultimately, our findings demonstrate that the light-driven H_2 evolution performance of porphyrin-based materials can be strategically amplified by fine-tuning intramolecular energy transfer between the π-linkers and the porphyrin core. This approach opens new avenues for optimizing light harvesting and charge separation within these systems. Furthermore, by systematically varying electron-rich or electron-deficient moieties as π-linkers bridging the anchoring groups and the porphyrin macrocycle, it becomes possible to precisely modulate electronic interactions and further elevate photocatalytic H_2 evolution. This molecular engineering strategy offers a versatile platform for the rational design of next-generation porphyrin conjugates with superior solar-to-hydrogen conversion efficiencies.

CONCLUSIONS

In this study, three porphyrin-based photosensitizers incorporating two 4-ethynylbenzoic acid, 3-ethynylbenzoic acid, or 5-ethynylthiophene-2-carboxylic acid tethered at the *meso*-position of the porphyrin macrocycle have been developed, designed, and synthesized. Their photophysical and electrochemical properties have been examined. The impact of attaching these sensitizing chromophores to colloidal TiO_2 on interfacial processes and PHE efficiencies has been investigated. The introduction of long-chain alkyloxy groups in the PS structure is suggested to generally slow down the charge recombination

process. The influence of π-spacers on the photophysical properties of porphyrin PSs for light-driven hydrogen energy conversion was studied. The results indicate that a single aromatic spacer improved the PHE performance due to an enhanced electron-donating ability from phenyl to thiophene structures. The PHE system with **PoTA3** exhibited the highest and most remarkable initial photocatalytic activity, with an initial apparent quantum yield % (AQY_i%) of 8.3% and an initial hydrogen production activity ($activity_i$) of 485 mmol g^{-1} h^{-1} under blue light irradiation. Both **PoTA1** and **PoTA3** showed distinct performances under white light irradiation, with AQY_i% values of 5.5% and 6.8% respectively, surpassing that of **YD2-*o*-C8** (AQY_i% = 4.07%) reported under the same photocatalytic conditions. The remarkable hydrogen evolution activity and long-term durability exhibited by these porphyrin-based PSs highlight their strong potential as foundational components in next-generation photocatalytic devices aimed at addressing global energy challenges. This work underscores the transformative promise of this structural framework for achieving broad-spectrum light absorption and enabling synergistic co-sensitization strategies. Looking ahead, such molecularly engineered PSs are poised to drive significant advances not only in solar-driven hydrogen generation from water but also in a wide array of emerging photocatalytic applications, paving the way for sustainable and versatile energy conversion technologies.

Received 30 July 2025; accepted 18 September 2025; published online 21 November 2025

1 Ahmad H, Kamarudin SK, Minggu LJ, *et al.* Hydrogen from photocatalytic water splitting process: a review. Renew Sustain Energy Rev, 2025, 43: 599–610
2 Dalle KE, Warnan J, Leung JJ, *et al.* Electro- and solar-driven fuel synthesis with first row transition metal complexes. Chem Rev, 2019, 119: 2752–2875
3 Le Goff A, Artero V, Jousselme B, *et al.* From hydrogenases to noble metal-free catalytic nanomaterials for H_2 production and uptake. Science, 2009, 326: 1384–1387
4 Cao S, Yu J. Carbon-based H_2-production photocatalytic materials. J PhotoChem PhotoBiol C-PhotoChem Rev, 2016, 27: 72–99
5 Xie G, Zhang K, Guo B, *et al.* Graphene-based materials for hydrogen generation from light-driven water splitting. Adv Mater, 2013, 25: 3820–3839
6 Ogden JM. Prospects for building a hydrogen energy infrastructure. Annu Rev Energy Environ, 1999, 24: 227–279
7 O'Neill JS, Kearney L, Brandon MP, *et al.* Design components of porphyrin-based photocatalytic hydrogen evolution systems: a review. Coord Chem Rev, 2022, 467: 214599
8 Cui R, Li W, Duan W, *et al.* Platinum co-catalysis modulation of exciton dynamics and film loading for durably photoactive benzyl alcohol value-added conversion and hydrogen co-production. Appl Catal B-Environ Energy, 2025, 378: 125571
9 Li W, Duan W, Liao G, *et al.* 0.68% of solar-to-hydrogen efficiency and high photostability of organic-inorganic membrane catalyst. Nat Commun, 2024, 15: 6763
10 Ma T, Liao G, Gao F, *et al.* Flexible hybrid membrane with synergistic exciton dynamics for excessive 280 h of durably piezo-photocatalytic H_2O-to-H_2 conversion. Small, 2024, 20: 2408056
11 Rahman MZ, Kibria MG, Mullins CB. Metal-free photocatalysts for hydrogen evolution. Chem Soc Rev, 2020, 49: 1887–1931
12 Banerjee T, Podjaski F, Kröger J, *et al.* Polymer photocatalysts for solar-to-chemical energy conversion. Nat Rev Mater, 2021, 6: 168–190
13 Wang H, Liu X, Niu P, *et al.* Porous two-dimensional materials for photocatalytic and electrocatalytic applications. Matter, 2020, 2: 1377–1413
14 Niu P, Dai J, Zhi X, *et al.* Photocatalytic overall water splitting by graphitic carbon nitride. InfoMat, 2021, 3: 931–961
15 Corredor J, Rivero MJ, Rangel CM, *et al.* Comprehensive review and future perspectives on the photocatalytic hydrogen production. J Chem Tech Biotech, 2019, 94: 3049–3063
16 Mohnani S, Bonifazi D. Supramolecular architectures of porphyrins on surfaces: The structural evolution from 1D to 2D to 3D to devices. Coord Chem Rev, 2010, 254: 2342–2362
17 Gilissen PJ, White PB, Berrocal JA, *et al.* Molecular motor-functionalized porphyrin macrocycles. Nat Commun, 2020, 11: 5291
18 Wakahara T, D'Angelo P, Miyazawa K', *et al.* Fullerene/cobalt porphyrin hybrid nanosheets with ambipolar charge transporting characteristics. J Am Chem Soc, 2012, 134: 7204–7206
19 Chou HH, Reddy KSK, Wu HP, *et al.* Influence of phenylethynylene of push-pull zinc porphyrins on the photovoltaic performance. ACS Appl Mater Interfaces, 2016, 8: 3418–3427
20 Dessì A, Calamante M, Mordini A, *et al.* Organic dyes with intense light absorption especially suitable for application in thin-layer dye-sensitized solar cells. Chem Commun, 2014, 50: 13952–13955
21 Yasin A, Nair VS, Assa Aravindh S, *et al.* *Meso*-Zn(II)porphyrins of tailored functional groups for intensifying the photoacoustic signal. J Mater Chem C, 2020, 8: 8546–8559
22 Brumbach MT, Boal AK, Wheeler DR. Metalloporphyrin assemblies on pyridine-functionalized titanium dioxide. Langmuir, 2009, 25: 10685–10690
23 Ladomenou K, Kitsopoulos TN, Sharma GD, *et al.* The importance of various anchoring groups attached on porphyrins as potential dyes for DSSC applications. RSC Adv, 2014, 4: 21379–21404
24 Clifford JN, Palomares E, Nazeeruddin MK, *et al.* Molecular control of recombination dynamics in dye-sensitized nanocrystalline TiO_2 films: free energy vs distance dependence. J Am Chem Soc, 2004, 126: 5225–5233
25 Palomares E, Martínez-Díaz MV, Haque SA, *et al.* State selective electron injection in non-aggregated titanium phthalocyanine sensitised nanocrystalline TiO_2 films. Chem Commun, 2004, 18: 2112–2113
26 Rochford J, Chu D, Hagfeldt A, *et al.* Tetrachelate porphyrin chromophores for metal oxide semiconductor sensitization: effect of the spacer length and anchoring group position. J Am Chem Soc, 2007, 129: 4655–4665
27 Rochford J, Galoppini E. Zinc(II) tetraarylporphyrins anchored to TiO_2, ZnO, and ZrO_2 nanoparticle films through rigid-rod linkers. Langmuir, 2008, 24: 5366–5374
28 Balzani V, Credi A, Venturi M. Photochemical conversion of solar energy. ChemSusChem, 2008, 1: 26–58
29 Fujishima A, Honda K. Electrochemical photolysis of water at a semiconductor electrode. Nature, 1972, 238: 37–38
30 Watanabe M. Dye-sensitized photocatalyst for effective water splitting catalyst. Sci Tech Adv Mater, 2017, 18: 705–723
31 Ho P, Mark MF, Wang Y, *et al.* Panchromatic sensitization with Zn^{II} porphyrin-based photosensitizers for light-driven hydrogen production. ChemSusChem, 2018, 11: 2517–2528
32 Yella A, Lee HW, Tsao HN, *et al.* Porphyrin-sensitized solar cells with cobalt (II/III)-based redox electrolyte exceed 12 percent efficiency. Science, 2011, 334: 629–634
33 Hagiwara H, Higashi K, Watanabe M, *et al.* Effect of porphyrin molecular structure on water splitting activity of a $KTaO_3$ photocatalyst. Catalysts, 2016, 6: 42
34 Tang Y, Wang Y, Li X, *et al.* Porphyrins containing a triphenylamine donor and up to eight alkoxy chains for dye-sensitized solar cells: a high efficiency of 10.9%. ACS Appl Mater Interfaces, 2015, 7: 27976–27985
35 Higashino T, Kawamoto K, Sugiura K, *et al.* Effects of bulky substituents of push-pull porphyrins on photovoltaic properties of dye-sensitized solar cells. ACS Appl Mater Interfaces, 2016, 8: 15379–15390
36 Harima Y, Fujita T, Kano Y, *et al.* Lewis-acid sites of TiO_2 surface for adsorption of organic dye having pyridyl group as anchoring unit. J Phys Chem C, 2013, 117: 16364–16370
37 Ooyama Y, Nagano T, Inoue S, *et al.* Dye-sensitized solar cells based on donor-π-acceptor fluorescent dyes with a pyridine ring as an electron-withdrawing-injecting anchoring group. Chem Eur J, 2011, 17: 14837–

14843
38 Ooyama Y, Inoue S, Nagano T, *et al*. Dye-sensitized solar cells based on donor-acceptor π-conjugated fluorescent dyes with a pyridine ring as an electron-withdrawing anchoring group. Angew Chem Int Ed, 2011, 50: 7429–7433
39 Angaridis PA, Ferentinos E, Charalambidis G, *et al*. Pyridyl vs. bipyridyl anchoring groups of porphyrin sensitizers for dye sensitized solar cells. RSC Adv, 2016, 6: 22187–22203
40 Ambre R, Chen KB, Yao CF, *et al*. Effects of porphyrinic *meso*-substituents on the photovoltaic performance of dye-sensitized solar cells: number and position of *p*-carboxyphenyl and thienyl groups on zinc porphyrins. J Phys Chem C, 2012, 116: 11907–11916
41 Abbotto A, Manfredi N, Marinzi C, *et al*. Di-branched di-anchoring organic dyes for dye-sensitized solar cells. Energy Environ Sci, 2009, 2: 1094–1101
42 Imahori H, Matsubara Y, Iijima H, *et al*. Effects of *meso*-diarylamino group of porphyrins as sensitizers in dye-sensitized solar cells on optical, electrochemical, and photovoltaic properties. J Phys Chem C, 2010, 114: 10656–10665
43 Campbell WM, Burrell AK, Officer DL, *et al*. Porphyrins as light harvesters in the dye-sensitised TiO_2 solar cell. Coord Chem Rev, 2004, 248: 1363–1379
44 Gouterman M. Spectra of porphyrins. J Mol Spectr, 1961, 6: 138–163
45 Jia QF, Chen PY, Cao J, *et al*. Anchored porphyrin with different side chain groups via its axial coordinate self-assembly for dye-sensitized solar cells. J PhotoChem PhotoBiol A-Chem, 2021, 410: 113125
46 Yella A, Mai C, Zakeeruddin SM, *et al*. Molecular engineering of push-pull porphyrin dyes for highly efficient dye-sensitized solar cells: the role of benzene spacers. Angew Chem Int Ed, 2014, 53: 2973–2977
47 Mathew S, Yella A, Gao P, *et al*. Dye-sensitized solar cells with 13% efficiency achieved through the molecular engineering of porphyrin sensitizers. Nat Chem, 2014, 6: 242–247
48 Gonuguntla S, Kamesh R, Pal U, *et al*. Dye sensitization of TiO_2 relevant to photocatalytic hydrogen generation: current research trends and prospects. J PhotoChem PhotoBiol C-PhotoChem Rev, 2023, 57: 100621
49 Li X, Yu J, Low J, *et al*. Engineering heterogeneous semiconductors for solar water splitting. J Mater Chem A, 2015, 3: 2485–2534
50 Chung I, Lee B, He J, *et al*. All-solid-state dye-sensitized solar cells with high efficiency. Nature, 2012, 485: 486–489
51 Haque SA, Palomares E, Cho BM, *et al*. Charge separation versus recombination in dye-sensitized nanocrystalline solar cells: the minimization of kinetic redundancy. J Am Chem Soc, 2005, 127: 3456–3462
52 Bessho T, Yoneda E, Yum JH, *et al*. New paradigm in molecular engineering of sensitizers for solar cell applications. J Am Chem Soc, 2009, 131: 5930–5934
53 Dong P, Hou G, Xi X, *et al*. WO_3-based photocatalysts: morphology control, activity enhancement and multifunctional applications. Environ Sci-Nano, 2017, 4: 539–557
54 Feng J, Yang F, Ye Y, *et al*. Surface-bound sacrificial electron donors in promoting photocatalytic reduction on titania nanocrystals. Nanoscale, 2019, 11: 19512–19519
55 Wen Y, Fan L, Yao X, *et al*. Development of triphenylamine derived photosensitizers for efficient hydrogen evolution from water. Chem Eur J, 2025, 31: e202404542
56 Lehn JM, Ziessel R. Photochemical generation of carbon monoxide and hydrogen by reduction of carbon dioxide and water under visible light irradiation. Proc Natl Acad Sci USA, 1982, 79: 701–704
57 Ziessel R, Hawecker J, Lehn J. Photogeneration of carbon monoxide and of hydrogen via simultaneous photochemical reduction of carbon dioxide and water by visible-light irradiation of organic solutions containing tris(2,2'-bipyridine)ruthenium(II) and cobalt(II) species as homogeneous catalysts. Helvetica Chim Acta, 1986, 69: 1065–1084
58 Lu J, Xu X, Cao K, *et al*. D–π–A structured porphyrins for efficient dye-sensitized solar cells. J Mater Chem A, 2013, 1: 10008

Acknowledgement This work was supported by the Hong Kong Research Grants Council (PolyU 123021/17P), the Environment and Conservation Fund (ECF 86/2021) from the Government of HKSAR, and the Hong Kong Polytechnic University (ZVVU and ZVXU).

Funding note Open Access funding provided by The Hong Kong Polytechnic University.

Author contributions Wen Y undertook responsibilities including conceptualization, data curation, formal analysis, investigation, methodology development, and drafting the original manuscript. Kwok Y Y was in charge of investigation, data curation, and formal analysis. Ho C-L assumed roles in data curation, funding acquisition, methodology design, project administration, resource coordination, validation, drafting the original manuscript, as well as manuscript review and editing.

Conflict of interest The authors declare that they have no conflict of interest.

Supplementary information Supplementary materials are available in the online version of the paper.

Cheuk-Lam Ho earned her BS and PhD degrees from Hong Kong Baptist University. Subsequently, she worked on her postdoctoral research at Hong Kong Baptist University and the University of Hong Kong. From 2012 to 2017, she served as a Research Assistant Professor at Hong Kong Baptist University. In 2017, she joined The Hong Kong Polytechnic University as an Assistant Professor and was promoted to Associate Professor in 2023. Her research interests include photocatalytic hydrogen generation, metallopolymers and metallophosphors for OLEDs and organic solar cells, dye-sensitized solar cells, as well as nanomaterials and related technologies.

基于分子工程策略开发兼具多锚定基团与烷氧基修饰的卟啉光敏剂以实现高效稳定的光催化制氢

温宇东[1,2], 何卓琳[1,2*], 郭欣宜[1,2]

摘要 在本研究中，我们推出了新一代卟啉基光敏剂**PoTA1–PoTA3**，其创新设计在于卟啉大环介观位点同时引入双锚定基团(4-乙炔基苯甲酸、3-乙炔基苯甲酸或5-乙炔基噻吩-2-甲酸)并修饰长链烷氧基取代基. 这种双修饰策略不仅有效抑制了电荷复合现象, 还减少了在二氧化钛表面的聚集效应. 值得注意的是, 具有5-乙炔基噻吩-2-甲酸结构的**PoTA3**表现出显著红移且宽化的吸收光谱, 实现了更优异的太阳光谱利用率. 在蓝光照射下, 基于**PoTA3**的体系在水介质中实现了8.3%的表观量子产率、485 mmol g^{-1} h^{-1}的初始析氢速率以及27,858的卓越转化数—这些性能指标均显著优于**PoTA1**和**PoTA2**. 更引人注目的是, 在相同操作条件下, **PoTA1**和**PoTA3**在白光照射下分别实现5.5%和6.8%的表观量子产率, 显著超越基准材料YD2-o-C8 (4.07%). **PoTA1**与**PoTA3**通过协同增强光捕获能力、抑制分子聚集以及优化HOMO与LUMO轨道电子密度分布, 最终实现了高效性与运行稳定性的统一. 这些发现为新一代太阳能-氢能转换系统创建了灵活的分子工程平台, 该研究策略为设计性能更优异的光敏剂开辟了新路径, 有望推动太阳光驱动水制氢技术的重大突破.

